Understanding energetic disorder in electron-deficient-core-based non-fullerene solar cells

Jun Yuan[1†], Chujun Zhang[2†], Honggang Chen[1,3], Can Zhu[1,3], Sin Hang Cheung[2], Beibei Qiu[3], Fangfang Cai[1], Qingya Wei[1], Wei Liu[1], Hang Yin[2], Rui Zhang[4], Jidong Zhang[5], Ye Liu[1], Huotian Zhang[4], Weifang Liu[1], Hongjian Peng[1], Junliang Yang[6], Lei Meng[3], Feng Gao[4], Shukong So[2], Yongfang Li[3] & Yingping Zou[1*]

[1]College of Chemistry and Chemical Engineering, Central South University, Changsha 410083, China;
[2]Department of Physics and Institute of Advanced Materials, Hong Kong Baptist University, Hong Kong, China;
[3]Beijing National Laboratory for Molecular Sciences, Institute of Chemistry, Chinese Academy of Sciences, Beijing 100190, China;
[4]Department of Physics, Chemistry and Biology (IFM), Linköping University, Linköping 58183, Sweden;
[5]State Key Laboratory of Polymer Physics and Chemistry, Changchun Institute of Applied Chemistry, Chinese Academy of Sciences, Changchun 130022, China;
[6]Hunan Key Laboratory for Super-microstructure and Ultrafast, Process School of Physics and Electronic, Changsha 410083, China

Recent advances in material design for organic solar cells (OSCs) are primarily focused on developing near-infrared non-fullerene acceptors, typically A-DA′D-A type acceptors (where A abbreviates an electron-withdrawing moiety and D, an electron-donor moiety), to achieve high external quantum efficiency while maintaining low voltage loss. However, the charge transport is still constrained by unfavorable molecular conformations, resulting in high energetic disorder and limiting the device performance. Here, a facile design strategy is reported by introducing the "wing" (alkyl chains) at the terminal of the DA′D central core of the A-DA′D-A type acceptor to achieve a favorable and ordered molecular orientation and therefore facilitate charge carrier transport. Benefitting from the reduced disorder, the electron mobilities could be significantly enhanced for the "wing"-containing molecules. By carefully changing the length of alkyl chains, the mobility of acceptor has been tuned to match with that of donor, leading to a minimized charge imbalance factor and a high fill factor (FF). We further provide useful design strategies for highly efficient OSCs with high FF.

non-fullerene organic solar cells, electron-deficient-core, energetic disorder, molecular design strategy

1 Introduction

Over the past three decades, the development of new organic materials has been driven by the desire to synthesize high performance organic photovoltaic materials for applications in bulk heterojunction (BHJ) organic solar cells (OSCs) [1–8]. Much advancement in this area has been made by the design of new classes of donor-acceptor (D-A) alternating conjugated molecules, which can offer the unique feature of tuning the electronic energy levels and the optical bandgap of the photovoltaic materials [9–11]. For a long period of time,

---

†These authors contributed equally to this work.
*Corresponding author (email: yingpingzou@csu.edu.cn)

because of the lack of high-performance n-type organic semiconductor acceptors that can compete with fullerene derivatives (*e.g.*, [6,6]-phenyl-C_{61}-butyric acid methyl ester (PCBM) and indene-C_{60}-bis-adduct (ICBA)) [12–14], most advances in the device performance came from the design of new p-type organic semiconductor donors [15–17]. Recently, the development of non-fullerene acceptors with absorption bands in the *Vis*-NIR range [18–27], such as A-DA′D-A type molecule Y6 [28], represents an exciting opportunity to solve this problem and leads to high power conversion efficiencies (PCEs) over 15%. However, it is still poorly understood, why A-DA′D-A-like molecule structure such as Y5 [29] or Y6 tend to perform significantly higher performance than the representative non-fullerene acceptor ITIC or IT-4F [30,31]. One phenomenon is the low voltage losses and high short-circuit current density of the OSCs with Y-series molecules as the acceptor [32–35], but this does not fully explain how these high performance materials can exhibit significantly high charge transport properties. While the determining factors for short-circuit current density (J_{SC}) and open-circuit voltage (V_{OC}) in OSCs have been relatively well understood, the structure and performance relationship in this high-performance photovoltaic system remains unclear, particularly in the relationship of structure of the photovoltaic materials and the fill factor (FF) of the OSCs. Various factors influencing FF have been discussed, among which the charge transport issue plays a critical role during the field-dependent extraction and recombination of free charge carriers. However, a systematic understanding of the relationship between the molecular structure and charge transport properties is still lacking. Therefore, improvements in the electronic properties of these promising photovoltaic materials require the understanding of fundamental transport process.

Charge carrier transport in organic semiconductors is affected by a degree of structural disorder in both the manifold of localized hopping sites and the local variations of molecular packing [36]. This structural disorder is strongly influenced by structural features, where a wide range of intra- and intermolecular interactions, and conformational diversity in a morphologically diverse film shows a huge impact on charge transport [37–39]. However, the vibration feature of organic semiconductor materials and the intense interaction between the adjacent electronic states makes the value of energetic disorder more difficult to control. Modification of the position or the size of alkyl side groups for molecular or polymeric materials has been shown to significantly affect the miscibility, solubility and thin film microstructure and hence performance in OSCs. For instance, by introducing alkyl groups in the backbone, the crystalline properties of the conjugated polymers can be improved, resulting in a well-defined morphology and optimized domain size in blended BHJ films. Several experimental and modeling studies have addressed that the energetic disorder was controlled through optimizing polymer structure to boost the charge carrier mobility, and subsequently the device electrical properties in organic field-effect transistors (OFETs) [40–43]. Nevertheless, the impacts of alkyl side chain on the conformational and energetic disorder in OSCs is barely studied and the fundamental reason is also far from being probed [44]. We aim to understand the molecular conformation that imparts intermolecular interactions and interchain electronic coupling, which can help charge transport and ultimately improve performance of organic photovoltaic devices. Our group [29] recently reported a series of organic solar cells based on Y5 as acceptor and J61 or PBDB-T or TTFQx-T1 as donor. The decreased energetic disorder, as extracted by temperature-dependent current density-voltage (*J-V*) and analyzed by Gaussian disorder model (GDM), was associated with the increased FF and ultimate PCE of the devices. To date, a comparison study on the charge transport behavior for different non-fullerene acceptors from the same family has yet to be established. In order to achieve in-depth understanding of the energetic disorder at an atomic level, its effects on the density of state (DOS) widths is critical for the further improvement of the charge transport properties of the A-DA′D-A acceptors [39,45].

Here, we have investigated the effects of alkyl side chains on the physicochemical and photovoltaic properties of a series of A-DA′D-A type non-fullerene acceptors (Y3, Y11 and Y18, Figure 1) with the same backbone but without (Y3) or with (Y11 and Y18) different alkyl side chains at the terminal of the DA′D central fused ring unit. We find that rotation of the end-group unit around central core of Y3 results in conformational and energetic disorder and therefore potentially limits charge transport of the acceptor and FF of the corresponding OSCs. Introducing the alkyl chains at the terminal of the central core in Y11 and Y18 limited the rotation torsion so that it eliminated the disorder and improved the charge carrier mobility. More interestingly, the length of the alkyl side chain in the A-DA′D-A acceptors is also correlated to the energetic disorder, leading to a regularly increase in the electron mobility as longer alkyl chains was connected. Detailed charge transport study of the OSCs based on the three acceptors reveals that Y18 with an optimized alkyl chain achieves reduced energetic disorder, a balanced field-dependent hole-to-electron ratios, leading to a high FF of 76.4% and PCE over 16% in the resulting device. In addition, the poor electron mobility originating from the higher energetic disorder in PM6:Y3 system shows a big impact on photovoltaic performance. Therefore, a ternary blend strategy inspired by the detailed transport study was used to improve charge transport properties in the BHJ films. Through introducing the third component acceptor $PC_{71}BM$, with a selecting role of balancing hole and electron transport in BHJs, the FF as well as PCE of the OSCs can be significantly enhanced. This work presents useful guidelines to
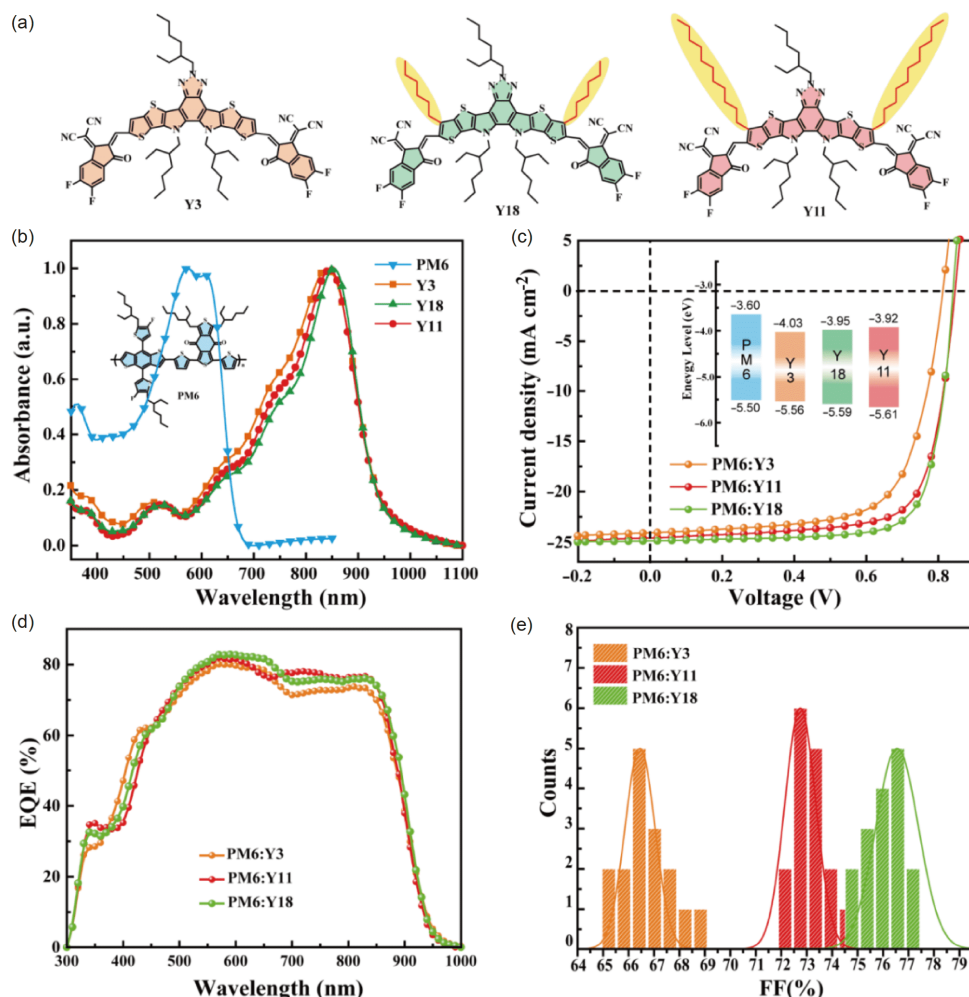
Figure 1 Properties and photovoltaic performance. (a) Chemical structures of acceptor molecules. (b) Normalized thin-film absorption of donor and acceptor molecules. Inset: the chemical structure of donor material. (c) *J-V* curves of BHJ solar cells with various acceptors. Inset: energy diagram for donor and acceptor molecules used in this study (Figure S7). (d) The EQE curves of BHJ solar cells with various acceptors. (e) Histogram of the PCE measurements for 15 devices based on BHJ solar cells with various acceptors (color online).

better understand the interplay between molecular design and the degree of energetic disorder that governs the charge transport properties in non-fullerene OSCs. Apart from molecular design, device engineering strategy has also been put forward to further improve device performances.

2   Results and discussion

The device based on PM6:Y3 blend film has been reported to exhibit high J_{SC} of 23.7 mA cm^{-2} and V_{OC} of 0.83 V while FF in this device only achieved a moderate value (65.6%) [46]. The FF is lower than that of other high performance non-fullerene OSCs, which imposes severe restrictions on the further enhancement of their PCEs [47]. It has become a consensus that the FF is mainly determined by the charge transport and recombination in the active layer. From the morphological point of view, the presence of low energetic

disorder regions in thin films can improve the charge transport properties due to the high degree of π-π stacking of backbone moieties and torsion-free molecular conformation of side chains. In order to understand the molecular conformation of Y3, we firstly conducted density functional theory (DFT) calculation. The potential rotamers TT-DFIC (DFIC=fluorinated dicyanomethylene) are extracted from the TT unit and DFIC. As shown in Figure S5(a, b), the optimized configuration for TT-DFIC shows a low energy difference of 1.05 kcal mol^{-1} between the conformations at 0° and 180°. This energy barrier is not high enough to achieve highly order conformations [40,41]. We hence, introduced two different lengths of alkyl chains (*n*-hexyl and *n*-undecyl) at the β position of the TT unit (Y11 [48] and Y18) (the synthetic routes of Y3, Y11 and Y18 are shown in Scheme S1, Supporting information online). The detailed synthetic processes and ^{1}H nuclear magnetic resonance (^{1}H NMR) spectra for Y18 are provided in Figures S1–S4

(Supporting information online).

Moreover, we further conducted temperature-dependent ¹H NMR to probe the molecular conformation of TT unit-based acceptor (Y3) and alkylated TT unit-based acceptor (Y11). Interestingly, the clear chemical shift of thiophene proton (H_b) on the TT unit (in d_3-chlorofrom) gradually moves from 8.25 to 8.17 ppm, upon decreasing temperature from 25 to −45 °C. The clear chemical shifts can be due to the rotation of H_b on the TT unit away from the carbonyl group of DFIC. It suggests that O–S geometry of TT-DFIC is a relatively stable conformation (less rotation tendency) at low temperature. In addition, the proton (H_a) on the C=C double bond linkage between central core and DFIC of Y3 is located on 9.03 ppm at room temperature. Nevertheless, the corresponding H_a' on Y11 as well as Y18 are located on ~9.16 ppm (Figure S4). The difference between H_a and H_a' may be from the formation of intramolecular non-covalent bonds between sulfur on the thiophene and carbonyl group [49,50]. It suggests that O–S geometry of TT-DFIC is a relatively stable conformation (less rotation tendency) at low temperature. As a result, one approach to minimize the conformational disorder of the backbone is the use of attractive interaction between sulfur and oxygen atom to form S···O interactions [51]. From the aspect of the DFT calculation, since the steric hindrance effect between the alkylated TT and DFIC significantly increase energy barriers, the terminal C–C bond (TT-DFIC) shows less rotation tendency (Figure S5(b, c)). In addition, a relatively stable conformation structure could be formed more easily by using alkylated TT, and hence, facilitate the electron transfer from donor to acceptor because the S···O noncovalent interaction can occur between the C=O group of DFIC and the TT group of the central core.

As shown in Figure 1(b), the three non-fullerene acceptors (NFAs) of Y3, Y11 and Y18 show similar optical bandgap (1.32 eV) in solid films and the absorption peaks (at 845–850 nm), which indicate effective intramolecular charge transfer between molecular backbones. The only difference between these three molecules is the structural disorder originated from the additional alkyl side chains. In order to reveal the underlying mechanism causing the difference of the charge transport, photothermal deflection spectroscopy (PDS) measurement was carried out to compare the subgap absorptions in the corresponding films. Generally, absorption energies larger than the bandgap are caused by band-to-band (highest occupied molecular (HOMO)-lowest unoccupied molecular (LUMO)) transition. The urbach energy can be calculated from the slope of the linear part of the absorption coefficient. From our PDS result (Figure S6), we found that Y3 demonstrates the largest urbach energy in band tail region as well as the conformational disorder [40,43,52].

The crystalline behavior of Y3, Y11 and Y18 neat and blend films were analyzed by using two-dimensional grazing incidence wide angle X-ray scattering (GIWAXS) (Figure S8). All three pristine films of Y3, Y18 and Y11 exhibit preferred face-on molecular packing, because of their obvious high ordered (100) diffraction peaks in the in-plane (IP) direction and π-π stacking diffraction peaks in out-of-plane (OOP) direction. The diffraction peaks of Y3, Y18 and Y11 in the in-plane (100) direction are located at 0.42, 0.42 and 0.41 Å⁻¹, respectively. Similarly, the diffraction peaks of Y3, Y18 and Y11 are also emerged in out-of-plane (100) and (010) orientation, and the π-π intermolecular d-spacing distances are 3.50, 3.63 and 3.63 Å, respectively. Compared with Y3, the π-π stacking peaks in q_z of Y11 and Y18 become stronger, meanwhile, the (100) diffraction peaks in q_r directions are also more obvious. The similar FWHM can be calculated (in range of 0.31–0.32) from the line cuts of pristine Y3, Y11 and Y18 films. The neat PM6 film presents a weaker π-π peak in OOP direction at q_z=1.68 Å⁻¹ and lamellar peaks in both IP and OOP directions at ~0.30 Å⁻¹. As shown in Figure S8, both blend films show a preferred face-on orientation with π-π stacking in the OOP direction (3.58, 3.63 and 3.76 Å for Y3, Y18 and Y11-based blend films, respectively). In the IP direction, the diffraction peak at q_r=0.30 Å⁻¹ could be the lamellar stacking of PM6. It is worth noting that the (100) diffraction peak of blend films also shown in in-plane direction, which was observed in the neat acceptor films. It can be seen that all the blend films have a similar diffraction peak of 0.54–0.59 Å⁻¹ at OOP direction, which might be enhanced by molecular packing originated from acceptors, according to the peak position of pure films illustrated in Figure S8. It is clear that introduction of alkyl chains induced higher crystallinity and more ordered packing, as evidenced by the sharper scattering peaks. Overall, the GIWAXS results indicate that within this Y-series NFA family with specific molecular geometry [53]: (1) introduction of the "wing" can increases the inter lamellar distance as expected; (2) variation in "wing" length on the β position of fused central core minimally affects the molecular face-on orientation. Transmission electron microscopy (TEM) can also be used to study the morphology of Y3, Y18 and Y11-based blend films. As shown in Figure S9, slightly larger aggregation could be observed in the PM6:Y18 and PM6:Y11 blend films. Thus, the morphological results, combined with the absorption spectra and external quantum efficiency (EQE) data, show that addition of the side chains can maintain a face-on orientation both in pristine and blend films (only a little difference on the distance of molecular packing). This is consistent with the DFT results of the TT-DFIC and alkylated TT-DFIC, in which a possible more ordered molecular structure could be formed after additional alkyl chains on TT unit. The alkyl side chains (steric effect) increase the non-covalent interaction between S and O atoms which had a positive effect on the stable conformation of NFA main chains. As well known, a torsion-free molecular

conformation of D-A conjugated main chains would have a more ordered self-organized structure. The alkylated TT-DFIC (Y11 and Y18) is demonstrated to form a relatively more ordered packing at the (010) direction during growth of crystallization along with the (100) direction. On the contrary, a relative disordered packing of D-A conjugated main chains resulted in weak ordered packing at the (100) direction for Y3. The long-range backbone ordering effectively extends electron transport pathway and therefore significantly improves the mobility. It seems reasonable that the incorporation of the alkyl side chains at the terminal of the fused central core unit could optimize transport behavior for either Y11 or Y18 so the FF of their corresponding OSCs could be improved.

To explore and compare the photovoltaic performance of the acceptors, BHJ OSCs were fabricated with an inverted configuration of ITO/ZnO/active layer/MoO$_3$/Ag, where poly[(2,6-(4,8-bis(5-(2-ethylhexyl)-4-fluorothiophen-2-yl)-benzo[1,2-*b*:4,5*b'*]-dithiophene)-*co*-(1,3-bis(thiophen-2-yl)-5,7-bis(2-ethylhexyl)benzo-[1,2-*c*:4,5-*c'*]dithiophene-4,8-dione))] (PM6) (Figure 1(b)) was chosen as the donor for complementary absorption with the acceptors. In order to eliminate unexpected changes in morphology due to additional post-processing steps, the active layers were prepared in the same blend ratios (donor/acceptor weight rations) and same thermal processing conditions. Figure 1(c) shows representative *J-V* curves of the OSCs under the illumination of standard AM 1.5 G, 100 mW cm^{-2}. Table 1 collects the average photovoltaic parameters (from at least fifteen devices) of these OSCs. As can be seen, all the OSCs generate a V_{OC} value from 0.81 to 0.84 V. Among these devices, the PM6:Y18-based OSC exhibits the highest FF (76.2%) while the smallest FF (65.6%) is found in the PM6:Y3 device. The device based on PM6:Y11 exhibits a comparable FF (73.5%) to that of the device based on PM6:Y18. All the OSCs exhibited J_{SC} higher than 24 mA cm^{-2} owing to their strong absorption in NIR (see absorbance spectra in Figure 1(b) and Figure S10). For the Y3 based device, although the V_{OC} and J_{SC} are similar to the devices based on Y11 and Y18, the FF lags behind them, resulting in a relatively low PCE (13.24%), while the PCEs of the Y11 and Y18 based devices are 15.27% and 16.02%, respectively.

Figure 1(d) shows the EQE spectra of the OSCs with a high and broad spectral response from 300 to 950 nm, indicating both the donor and acceptor simultaneously contribute to the overall photocurrent. The EQE response of the Y11 and Y18-based OSCs are stronger than that of the Y3 based device in the region of 660–860 nm, resulting in a slightly higher J_{SC} values. The calculated J_{SC} values integrated from the EQE spectra are 24.08, 24.58 and 24.89 mA cm^{-2} for the Y3, Y11 and Y18-based OSCs, respectively, which is consistent with the J_{SC} values measured from *J-V* curves (the deviation is within 1%).

To understand the origin of the FF variation of the OSCs based on the three A-DA'D-A non-fullerene acceptors, we firstly investigated charge transport properties of their BHJ films by space-charge-limited-current (SCLC) method. The principle of SCLC has been well documented elsewhere [54]. Hole and electron carriers mobilities were evaluated. Figure 2(a, b) shows the *J-V* characteristics of zero field hole and electron mobility ($\mu_{0,h}/\mu_{0,e}$). The detailed transport parameters of the BHJ films were summarized in Table 2. At room temperature, BHJ films with different acceptors (variation in length of alkyl side chain) show only small impacts on the hole transport, $\mu_{0,h}$ values are in range of 3×10^{-4} to 4×10^{-4} cm^2 V^{-1} s^{-1}. This phenomenon indicates that hole transporting pathways in the BHJ blends are mainly determined by donor material. Therefore, hole mobility is insensitive to the conformational change of acceptors. For the electron transport, one striking feature is that $\mu_{0,e}$ increases gradually when longer alkyl side chain was connected at the TT units of the central fused ring in the acceptor. The Y3 (without the alkyl side chain)-based BHJ film showed the lowest electron mobility (7.5×10^{-5} cm^2 V^{-1} s^{-1}). By contrast, the $\mu_{0,e}$ value shows about one order increase to 4.0×10^{-4} cm^2 V^{-1} s^{-1} for the Y18 (with *n*-hexyl side chains)-based and 6.2×10^{-4} cm^2 V^{-1} s^{-1} for the Y11 (with *n*-undecyl side chains)-based BHJ films, respectively. The higher electron mobilities in the PM6:Y18 and PM6:Y11 BHJ blends suggested that a continuous pathway was constructed for electron transport after alkyl TT-DFIC units was introduced in the molecular backbone. The long-range order backbone orientation contributes to an enhanced electron hopping rate between neighboring molecules.

As shown above, acceptors (Y18 and Y11) with alkyl TT-DFIC unit have higher electron mobility in such BHJ films due to more stable molecular conformation and rigid backbone. The mobility in OSC devices influences charge transport and recombination, consequently affecting the device performance, especially the FF, since the FF is dominated by the competition between charge collection and recombination. A high FF requires balanced mobilities of electrons and holes. Figure 2(c) shows electron and hole mobilities of the PM6 based films with different acceptors. The hole-to-electron mobility ratio at zero-field $\mu_{(0,h)}/\mu_{(0,e)}$ and corresponding FF of the OSCs were shown in Table 2. The PM6:Y18 BHJ with a $\mu_{(0,h)}/\mu_{(0,e)}$ ratio of 1.07, which performs more balanced zero-field mobility than PM6:Y3 and PM6:Y11 BHJ films, and therefore, resulting in the highest FF value of 76.4% in the OSCs. Furthermore, charge-carrier transport in disordered organic semiconductor, in particular, in organic BHJ system is electric field dependent. Generally, BHJ blends possess better balanced field-dependent transport which would account for the enhanced FF [55]. Here, the field dependent carrier mobilities for electron or hole in a given BHJ blend can be
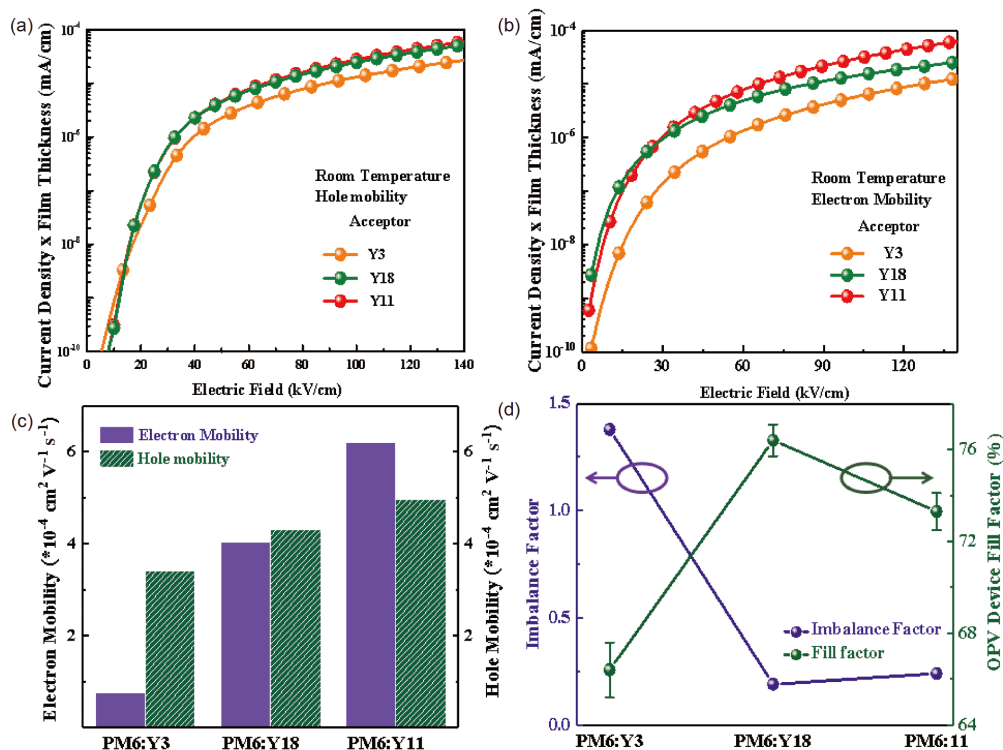
Figure 2 Charge mobilities of blend films. *J-V* characteristic of PM6-based BHJ films with different acceptors at room temperature in a semilog plot: (a) hole; (b) electron zero-field. (c) Hole and electron mobilities of PM6:acceptor BHJ films. The solid lines denote the best fit to SCLC model. (d) Charge imbalance factor (*Δ*) of PM6:acceptor BHJ and their corresponding device fill factor (color online).

Table 1 Photovoltaic performance of the PM6:acceptors (1:1.5, *w*/*w*) based devices

Devices [a]	V_{OC} (V)	J_{SC} (mA cm^{-2})	FF (%)	PCE (%)
PM6:Y3	0.81±0.01	24.10±0.71	66.4±1.2	13.24±0.52
PM6:Y11	0.84±0.01	24.62±0.33	73.3±0.8	15.27±0.48
PM6:Y18	0.84±0.00	24.91±0.45	76.4±0.7	16.02±0.35

a) Statistical data obtained from 15 independent devices under AM 1.5 G illumination at 100 mW cm^{-2}.

Table 2 Charge transport parameter of PM6:acceptor BHJ films. $\mu_{(0,293.7k)}$ and β represent the zero-field hole/electron mobility and the Poole-Frenkel factor at room temperature, imbalance factor Δ defined by Eq. (1), $\mu_{(0,h)}/\mu_{(0,e)}$ the ratio of hole and electron mobility at open-circuit (zero-field) at room temperature, and the corresponding device fill factor of three PM6:acceptor devices

Device	Electron/Hole	$\mu_{(0,293.7k)}$ (cm^2 V^{-1} s^{-1})	β (10^{-3} cm$^{1/2}$ V$^{-1/2}$)	Δ	$\mu_{(0,h)}/\mu_{(0,e)}$	Energetic disorder (meV)	FF (%)
PM6:Y3	Electron	7.5×10^{-5}	3.2	1.38	4.53	71	66.4
	Hole	3.4×10^{-4}	0.8			52	
PM6:Y18	Electron	4.0×10^{-4}	2.9	0.19	1.07	53	76.4
	Hole	4.3×10^{-4}	2.1			54	
PM6:Y11	Electron	6.2×10^{-4}	0.4	0.24	0.79	51	73.3
	Hole	4.9×10^{-4}	1.7			57	

described by the Poole-Frenkel (PF) model:

$$\mu(F) = \mu_0 \exp(\beta F^{1/2}) \tag{1}$$

where μ_0 is the zero-field charge mobility for electron and hole, F is the applied electric field and β is the associated Poole-Frenkel slope. μ_0 and F for both hole and electron in the PM6: acceptor BHJ blends was extracted from Eq. (1) to simulate charge carrier transport in different electric fields.

The plot of electric field dependent hole-to-electron mobilities based on PF model was given in Figure S11. The electric field range between open-circuit condition (*F*=0) to short-circuit condition ($F_{JSC}=V_{OC}/d$, *d* is the sample thickness) was defined to characterize the device relevant mobilities in BHJ blend. For the three PM6: acceptor devices, V_{OC} of the OSCs are around 0.81–0.83 V, and the optimized active layer thickness is 100 nm. Therefore, the square root of

applied electric field region of the PM6-based devices is $\sqrt{V/d} \approx 288$ (V$^{1/2}$ m$^{-1/2}$). Below, the imbalance factor (Δ) was evaluated to quantify hole and electron transport properties under a given electric field as:

$$\Delta = \frac{1}{F_{JSC}}\left\{ \int_0^{F_c}\left|\left(\frac{\mu_h}{\mu_e}\right)-1\right| \times dF + \int_{F_c}^{F_{JSC}}\left|\left(\frac{\mu_e}{\mu_h}\right)-1\right| \times dF\right\} \qquad (2)$$

where F_{JSC} is the applied electric field in the short circuit condition, and F_c is the electric field that hole and electron performed the same mobility. Figure 2(d) shows the Δ values of PM6-based BHJs and FFs in their corresponding devices. An anticorrelation can be clearly observed between the Δ and FF values. The PM6:Y3 blend has the largest Δ value of 1.8 due to the significant reduced electron mobility in the low electric field region, and therefore, the FF of the relevant OSCs device is only 66.4%. By contrast, the PM6:Y18 films demonstrate the smallest Δ of 0.19 indicating that hole and electron transport reached particular balance in OSC region. Accordingly, the Y18-based device achieves the highest FF of 76.4% among three OSCs devices. Although the balanced mobility does not ensure a perfect FF in all OSC devices, it still provides a qualitative explanation for the FF variation among our three devices, which are fabricated with the same donor and the similar acceptors.

To further understand transport properties in BHJ films, temperature dependent *J-V* measurements were performed for both hole and electron (see Figure S12). The transport data were then analyzed by GDM [56]. The hole energetic disorder σ_h and electron energetic disorder σ_e can be extracted using GDM as shown in the following equation:

$$\mu_0 = \mu_\infty \exp\left[-\left(\frac{2\sigma}{3kT}\right)^2\right] \qquad (3)$$

where μ_0 is the zero-field mobility, the high-temperature-limited carrier mobility, the Boltzmann constant, σ the energetic disorder [57]. Figure 3(a, b) shows the resulting plots for the hole and electron energetic disorder measurement of the three blend films, detailed hole and electron disorder parameter was given in Table 2. For comparison, we note that the σ_h values of the three BHJ films are quite concentrated, ranging from 52 to 57 meV. However, the σ_e (71 meV) in the Y3-based BHJ film is much higher than that of the other two alkyl TT-DFIC-based BHJ films, indicating that the electron energetic disorder is sensitive to the length of the alkyl side chains. As a result, Y11 (with *n*-undecyl side chain)-based BHJ achieves the lowest energetic disorder with the value of 51 meV. In the GDM, the charge carriers transport through a disorder molecular material by hopping through Gaussian distributed density-of-states (DOS) [58], which was demonstrated in Figure 3(c). The results clearly indicate that the reason for the poor electron mobility in the Y3-based BHJ is the broadening spreading of electron hop-

ping sites in LUMO orbital of Y3 molecule. Then the correlation between the energetic disorder and conformation diversity can be further explored. Many pervious reports suggested that local variations of molecular packing generated by random packing constraints would give rise to different intermolecular interactions, which would give rise to the disorder variation. In this respect, the presence of well-ordered acceptor material is expected to exhibit relatively narrow ^{1}H NMR signal, whereas the disordered organic
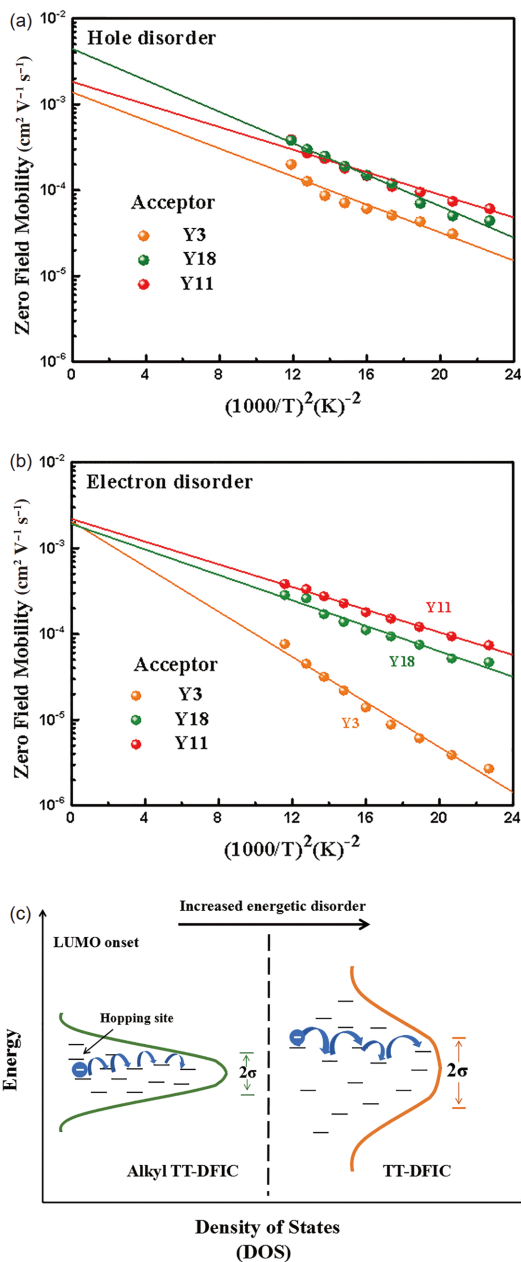
Figure 3 Energetic disorder of blend films. GDM analysis for PM6 based BHJ films: (a) hole, and (b) electron zero-field mobilities *versus* the square of reciprocal temperature. Solid lines are the best linear fits to the experimental data. Energetic disorder σ and high-temperature-limited mobility μ_∞ can be extracted from the slopes and *y*-intercept of the data plots. (c) Schematic illustration of the impact of with or without alkyl side chains on the electron transport and energetic disorder (color online).

molecule presents relatively broad signals that manifest distributions of molecular conformations associated with the backbone moieties. As shown in Figure S2(c) and Table S1, the broad ^{1}H NMR signal at 9.03 ppm is attributed to the C=C double bonds (H_a) linkage between central core and DFIC of Y3 with the average of integrals of full width at half maxima (FWHM) at 8.53. The narrow ^{1}H NMR signal centered at 9.08 ppm is attributed to the C=C (H_a') of Y11, exhibiting the FWHM at 4.47. Thus, the quantitative ^{1}H NMR analyses showed that the alkylated acceptor molecules such as Y11 have relatively higher fraction of ordered conformation regions, compared to the acceptor molecule Y3 without the alkyl side chains, which is consistent with the measured differences in their transport properties. Overall, these results suggest that the torsional flexibility of the Y3 molecular backbones contributes to the large electron energetic disorder and therefore, poor transport properties in the Y3-based BHJ blend. The molecular chains with low energy barrier correspond to the non-rigid molecular orientation, which consequently further increase the disorder. Thus, these sources of disorder can be largely removed when using alkyl TT-DFIC molecular structure with large energy barrier and low torsional flexibility.

The results presented above suggest an intrinsic and molecular origin of large electron energetic disorder in Y3. Since the potential rotamers from the TT unit and DFIC, the Y3 based blend film exhibited relatively larger Δ than the two blend films based on the acceptors Y11 and Y18 with alkyl side chains. One can therefore consider adding the higher electron mobility acceptor into the PM6:Y3 system to further enhance the device performance. The effects of PCBM in ternary blend were well studied. This effect was presumably because PCBM acts as electron transport channels in the ternary device which improves the electron mobility, and meanwhile PCBM may phase separate the binary material and suppress the non-radiative loss [59,60]. As seen from Figure S13, by introducing $PC_{71}BM$ into PM6:Y3 film, the electron mobilities of the PM6:Y3 blends were gradually increased from 7.5×10^{-5} to 3.8×10^{-4} cm^2 V^{-1} s^{-1} after adding $PC_{71}BM$, while the hole mobilities of the ternary blends were changed only a little bit after the acceptor $PC_{71}BM$ was introduced (from 3.4 to 3.6×10^{-4} cm^2 V^{-1} s^{-1}). The ternary solar cells are fabricated using an inverted structure (Figure 4(a)) and detailed performance are shown in Figure 4(b, c).
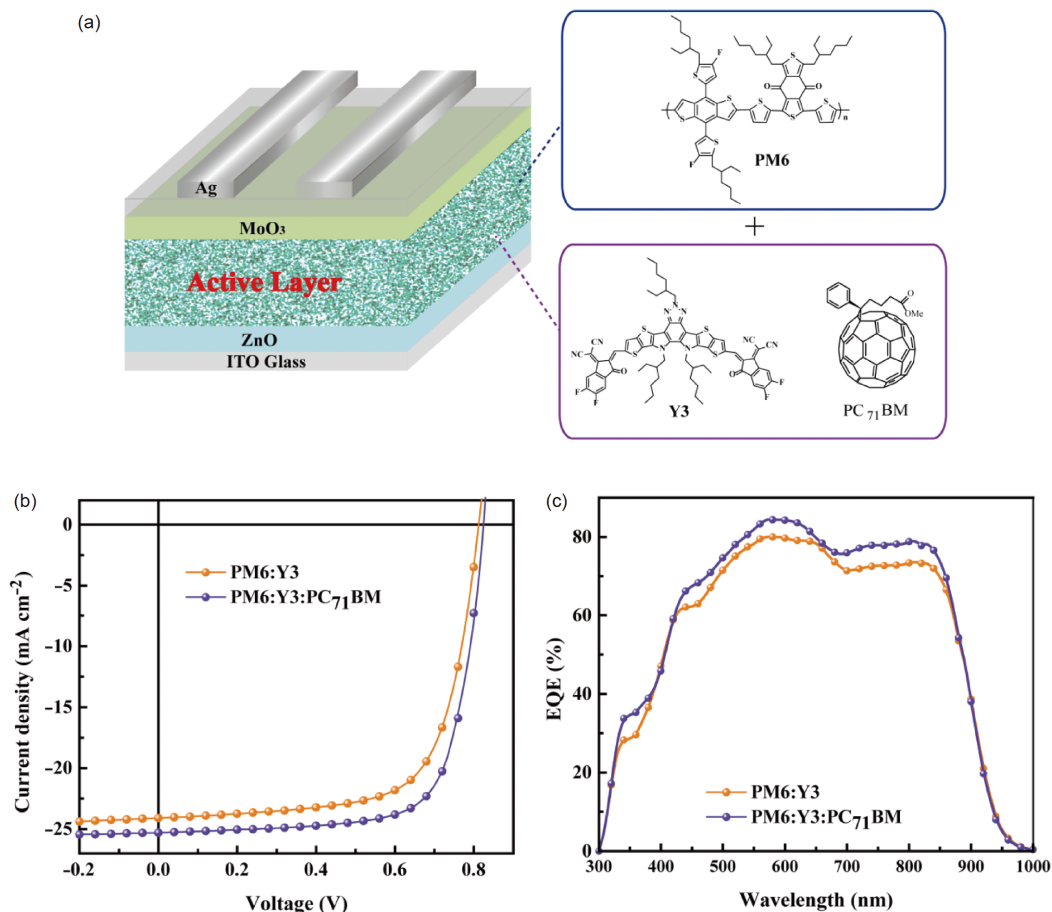

Figure 4 Efficient ternary solar cells. (a) Device architecture of the ternary solar cells. (b) *J-V* characteristics and (c) EQE spectra of the binary and ternary solar cells under illumination of an AM 1.5 G at 100 mW cm^{-2} (color online).

The PM6:Y3:PC$_{71}$BM (1:1.3:0.2) exhibited a V_{OC} of 0.82 V, J_{SC} of 25.3 mA cm^{-2} and FF of 73.1%, resulting in a higher PCE of 15.3%. It is highly encouraging that an effective strategy by optimizing the Δ between hole and electron mobility could enhance the performance of ternary OSCs.

3   Conclusions

In summary, we reported a detail study on a series of similar backbone A-DA′D-A type non-fullerene acceptors (Y3, Y11 and Y18), exploring how both the charge transport properties as well as the device performance are affected by tuning their molecular structure. Through both experimental and theoretical analysis, we uncover that torsional conformation of Y3 molecular backbone limits its charge transport properties and photovoltaic performance. By introducing the "wing" (alkyl chains) at the terminal of the central core of Y3 to achieve a high degree unified molecular conformation, the transport behavior can be significantly optimized in the BHJ films. Since this strategy would guarantee reduced energetic disorders for electron transport and a balanced transport, the PCE of the OSCs based on the optimized acceptors, Y11 and Y18, can achieve high PCEs of 15.27% and 16.02% along with improved fill factor, respectively (Table S2). In addition, we provide a feasible way that aims to increase the performance of Y3-based device: the ternary strategy of using a third component acceptor, with a selecting role of balancing hole and electron transport in BHJs. These findings give insights into how photovoltaic parameters are affected by molecular conformation, energetic disorder and charge transport properties and guiding the future molecular design of high-performance A-DA′D-A type non-fullerene acceptors.

Conflict of interest   The authors declare that they have no conflict of interest.

Supporting information   The supporting information is available online at http://chem.scichina.com and http://link.springer.com/journal/11426. The supporting materials are published as submitted, without typesetting or editing. The responsibility for scientific accuracy and content remains entirely with the authors.

1   Yu G, Gao J, Hummelen JC, Wudl F, Heeger AJ. *Science*, 1995, 270: 1789–1791
2   Li G, Zhu R, Yang Y. *Nat Photon*, 2012, 6: 153–161
3   Lu L, Zheng T, Wu Q, Schneider AM, Zhao D, Yu L. *Chem Rev*, 2015, 115: 12666–12731
4   Zhang ZG, Li Y. *Sci China Chem*, 2015, 58: 192–209
5   Kaltenbrunner M, White MS, Głowacki ED, Sekitani T, Someya T, Sariciftci NS, Bauer S. *Nat Commun*, 2012, 3: 770
6   Brabec CJ, Heeney M, McCulloch I, Nelson J. *Chem Soc Rev*, 2011, 40: 1185–1199
7   Peet J, Heeger AJ, Bazan GC. *Acc Chem Res*, 2009, 42: 1700–1708
8   Thompson BC, Fréchet JMJ. *Angew Chem Int Ed*, 2008, 47: 58–77
9   Yao H, Ye L, Zhang H, Li S, Zhang S, Hou J. *Chem Rev*, 2016, 116: 7397–7457
10   Zhou H, Yang L, You W. *Macromolecules*, 2012, 45: 607–632
11   Wu JS, Cheng SW, Cheng YJ, Hsu CS. *Chem Soc Rev*, 2015, 44: 1113–1154
12   He Y, Li Y. *Phys Chem Chem Phys*, 2011, 13: 1970–1983
13   He Y, Chen HY, Hou J, Li Y. *J Am Chem Soc*, 2010, 132: 1377–1382
14   Cheng YJ, Hsieh CH, He Y, Hsu CS, Li Y. *J Am Chem Soc*, 2010, 132: 17381–17383
15   Yuan J, Qiu L, Zhang Z, Li Y, He Y, Jiang L, Zou Y. *Chem Commun*, 2016, 52: 6881–6884
16   Liu D, Wang J, Gu C, Li Y, Bao X, Yang R. *Adv Mater*, 2018, 30: 1705870
17   Bin H, Zhang ZG, Gao L, Chen S, Zhong L, Xue L, Yang C, Li Y. *J Am Chem Soc*, 2016, 138: 4657–4664
18   Yan C, Barlow S, Wang Z, Yan H, Jen AKY, Marder SR, Zhan X. *Nat Rev Mater*, 2018, 3: 18003
19   Cheng P, Li G, Zhan X, Yang Y. *Nat Photon*, 2018, 12: 131–142
20   Xia T, Cai Y, Fu H, Sun Y. *Sci China Chem*, 2019, 62: 662–668
21   Hou J, Inganäs O, Friend RH, Gao F. *Nat Mater*, 2018, 17: 119–128
22   Wu Y, Zheng Y, Yang H, Sun C, Dong Y, Cui C, Yan H, Li Y. *Sci China Chem*, 2019, 63: 265–271
23   Baran D, Ashraf RS, Hanifi DA, Abdelsamie M, Gasparini N, Röhr JA, Holliday S, Wadsworth A, Lockett S, Neophytou M, Emmott CJM, Nelson J, Brabec CJ, Amassian A, Salleo A, Kirchartz T, Durrant JR, McCulloch I. *Nat Mater*, 2017, 16: 363–369
24   Meng D, Sun D, Zhong C, Liu T, Fan B, Huo L, Li Y, Jiang W, Choi H, Kim T, Kim JY, Sun Y, Wang Z, Heeger AJ. *J Am Chem Soc*, 2016, 138: 375–380
25   He D, Zhao F, Xin J, Rech JJ, Wei Z, Ma W, You W, Li B, Jiang L, Li Y, Wang C. *Adv Energy Mater*, 2018, 8: 1802050
26   Xiao B, Tang A, Zhang J, Mahmood A, Wei Z, Zhou E. *Adv Energy Mater*, 2017, 7: 1602269
27   Sun H, Liu T, Yu J, Lau TK, Zhang G, Zhang Y, Su M, Tang Y, Ma R, Liu B, Liang J, Feng K, Lu X, Guo X, Gao F, Yan H. *Energy Environ Sci*, 2019, 12: 3328–3337
28   Yuan J, Zhang Y, Zhou L, Zhang G, Yip HL, Lau TK, Lu X, Zhu C, Peng H, Johnson PA, Leclerc M, Cao Y, Ulanski J, Li Y, Zou Y. *Joule*, 2019, 3: 1140–1151
29   Yuan J, Zhang Y, Zhou L, Zhang C, Lau TK, Zhang G, Lu X, Yip HL, So SK, Beaupré S, Mainville M, Johnson PA, Leclerc M, Chen H, Peng H, Li Y, Zou Y. *Adv Mater*, 2019, 31: e1807577
30   Lin Y, Wang J, Zhang ZG, Bai H, Li Y, Zhu D, Zhan X. *Adv Mater*, 2015, 27: 1170–1174
31   Zhang Y, Yao H, Zhang S, Qin Y, Zhang J, Yang L, Li W, Wei Z, Gao F, Hou J. *Sci China Chem*, 2018, 61: 1328–1337
32   Yuan J, Huang T, Cheng P, Zou Y, Zhang H, Yang JL, Chang SY, Zhang Z, Huang W, Wang R, Meng D, Gao F, Yang Y. *Nat Commun*, 2019, 10: 570
33   Ma R, Liu T, Luo Z, Guo Q, Xiao Y, Chen Y, Li X, Luo S, Lu X, Zhang M, Li Y, Yan H. *Sci China Chem*, 2020, 63: 325–330
34   Fan B, Zhang D, Li M, Zhong W, Zeng Z, Ying L, Huang F, Cao Y. *Sci China Chem*, 2019, 62: 746–752
35   Luo Z, Sun R, Zhong C, Liu T, Zhang G, Zou Y, Jiao X, Min J, Yang C. *Sci China Chem*, 2020, 63: 361–369
36   Bässler H. *Phys Stat Sol (b)*, 1993, 175: 15–56
37   Shi X, Nadazdy V, Perevedentsev A, Frost JM, Wang X, von Hauff E, MacKenzie RCI, Nelson J. *Phys Rev X*, 2019, 9: 021038
38   Mendels D, Tessler N. *Sci Rep*, 2016, 6: 29092
39   Collins SD, Proctor CM, Ran NA, Nguyen TQ. *Adv Energy Mater*,

2016, 6: 1501721

40 Venkateshvaran D, Nikolka M, Sadhanala A, Lemaur V, Zelazny M, Kepa M, Hurhangee M, Kronemeijer AJ, Pecunia V, Nasrallah I, Romanov I, Broch K, McCulloch I, Emin D, Olivier Y, Cornil J, Beljonne D, Sirringhaus H. *Nature*, 2014, 515: 384–388

41 Zhang W, Smith J, Hamilton R, Heeney M, Kirkpatrick J, Song K, Watkins SE, Anthopoulos T, McCulloch I. *J Am Chem Soc*, 2009, 131: 10814–10815

42 Dong T, Lv L, Feng L, Xia Y, Deng W, Ye P, Yang B, Ding S, Facchetti A, Dong H, Huang H. *Adv Mater*, 2017, 29: 1606025

43 Nikolka M, Hurhangee M, Sadhanala A, Chen H, McCulloch I, Sirringhaus H. *Adv Electron Mater*, 2018, 4: 1700410

44 Bristow H, Thorley KJ, White AJP, Wadsworth A, Babics M, Hamid Z, Zhang W, Paterson AF, Kosco J, Panidi J, Anthopoulos TD, McCulloch I. *Adv Electron Mater*, 2019, 5: 1900344

45 Karki A, Wetzelaer G-AH, Reddy GNM, Nádaždy V, Seifrid M, Schauer F, Bazan GC, Chmelka BF, Blom PWM, Nguyen T. *Adv Funct Mater*, 2019, 29: 1901109

46 Wang R, Yuan J, Wang R, Han G, Huang T, Huang W, Xue J, Wang HC, Zhang C, Zhu C, Cheng P, Meng D, Yi Y, Wei KH, Zou Y, Yang Y. *Adv Mater*, 2019, 31: 1904215

47 Zheng Z, Hu Q, Zhang S, Zhang D, Wang J, Xie S, Wang R, Qin Y, Li W, Hong L, Liang N, Liu F, Zhang Y, Wei Z, Tang Z, Russell TP, Hou J, Zhou H. *Adv Mater*, 2018, 30: 1801801

48 Liu S, Yuan J, Deng W, Luo M, Xie Y, Liang Q, Zou Y, He Z, Wu H, Cao Y. *Nat Photonics*, 2020, doi: 101038/s41566-019-0573-5

49 Gao H, Sun Y, Cai Y, Wan X, Meng L, Ke X, Li S, Zhang Y, Xia R, Zheng N, Xie Z, Li C, Zhang M, Yip H, Cao Y, Chen Y. *Adv Energy Mater*, 2019, 9: 1901024

50 Zhang Z, Yu J, Yin X, Hu Z, Jiang Y, Sun J, Zhou J, Zhang F, Russell TP, Liu F, Tang W. *Adv Funct Mater*, 2018, 28: 1705095

51 Yu ZP, Liu ZX, Chen FX, Qin R, Lau TK, Yin JL, Kong X, Lu X, Shi M, Li CZ, Chen H. *Nat Commun*, 2019, 10: 2152

52 Kronemeijer AJ, Pecunia V, Venkateshvaran D, Nikolka M, Sadhanala A, Moriarty J, Szumilo M, Sirringhaus H. *Adv Mater*, 2014, 26: 728–733

53 Perdigón-Toro L, Zhang H, Markina A, Yuan J, Hosseini S, Wolff C, Zuo G, Stolterfoht M, Zou Y, Gao F, Andrienko D, Shoaee S, Neher D. *Adv Mater*, 2020, doi: 101002/adma201906763

54 Ho CHY, Cheung SH, Li HW, Chiu KL, Cheng Y, Yin H, Chan MH, So F, Tsang SW, So SK. *Adv Energy Mater*, 2017, 7: 1602360

55 Yin H, Bi P, Cheung SH, Cheng WL, Chiu KL, Ho CHY, Li HW, Tsang SW, Hao X, So SK. *Sol RRL*, 2018, 2: 1700239

56 Pasveer WF, Cottaar J, Tanase C, Coehoorn R, Bobbert PA, Blom PWM, de Leeuw DM, Michels MAJ. *Phys Rev Lett*, 2005, 94: 206601

57 Lee HKH, Li Z, Constantinou I, So F, Tsang SW, So SK. *Adv Energy Mater*, 2014, 4: 1400768

58 Borsenberger PM, Bässler H. *J Chem Phys*, 1991, 95: 5327–5331

59 Yu R, Yao H, Cui Y, Hong L, He C, Hou J. *Adv Mater*, 2019, 31: 1902302

60 Zhou Z, Xu S, Song J, Jin Y, Yue Q, Qian Y, Liu F, Zhang F, Zhu X. *Nat Energy*, 2018, 3: 952–959